Engineering Geology 329 (2024) 107387

Contents lists available at ScienceDirect

Engineering Geology

journal homepage: www.elsevier.com/locate/enggeo

Complex landslide patterns explained by local intra-unit variability of stratigraphy and structure: Case study in the Tyee Formation, Oregon, USA

Sean R. LaHusen [a,*], Alex R.R. Grant [b]

[a] U.S. Geological Survey, Geology, Minerals, Energy, and Geophysics Science Center, Moffett Field, CA, United States of America
[b] U.S. Geological Survey, Earthquake Science Center, Seattle, WA, United States of America

ARTICLE INFO

Keywords:
Landslides
Susceptibility
Stratigraphy
Geologic structure
Lithology
Geomorphology
Hazards

ABSTRACT

Lithology and geologic structure are important controls on landslide susceptibility and are incorporated into many regional landslide hazard models. Typically, metrics for mapped geologic units are used as model input variables and a single set of values for material strength are assumed, regardless of spatial heterogeneities that may exist within a map unit. Here we describe how differences in bedding thickness, grain size, inferred uniaxial compressive strength, and bedding dip control the inherent susceptibility of slopes to deep-seated failure within a single mapped geologic unit - the Tyee Formation of Oregon, USA. The Tyee, which covers over 15,000 km^2 and underlies much of the Oregon Coast Range, comprises gently folded alternating beds of sandstone and siltstone deposited as turbidites, forming a 2-km thick Eocene submarine fan which has been uplifted and exhumed through the Cenozoic. Deep-seated landslides are widespread in the Tyee, but form a complex spatial pattern such that landslide density ranges from 0 to 24% of the total landscape area. These slides are often extensive and sufficiently deep to reduce local hillslope gradients, resulting in a strong negative correlation between landslide density and mean local slope. Mean annual precipitation and predicted strong ground motions from Cascadia earthquake scenarios also fail to explain the spatial distribution of deep-seated landslides. Consequently, landslide stability models, which are strongly influenced by landscape slope, pore-water pressure, and seismic acceleration, yield landslide susceptibility maps which are broadly anti-correlated with mapped deep-seated landslide density. Through a multivariable linear regression model, we show that much of the variance in deep-seated landslide density can be explained by variability of intra-unit stratigraphic and structural characteristics, which we measure at 128 sites across two study areas totaling ~3000 km^2. Our results suggest bedding dip is only weakly correlated to landslide density, but strongly influences landslide failure style. Subtle increases in bedding dip, even in the gently folded Tyee Formation, result in a substantially higher likelihood of a landslide being cataclinal, or parallel to bedding. Overall, we find a slight majority of landslides fail within these cataclinal slopes, and that these landslides tend to be larger than non-cataclinal landslides. We also show that the lithological and structural properties that influence landslide susceptibility are distinct for these two populations of landslides. Our results demonstrate how localized, intra-unit, geologic variability can exert strong control on landslide susceptibility and failure style. This suggests that in some locations, landslide hazard models could be significantly improved by incorporating detailed, spatially variable, geologic properties rather than relying solely on generalized geologic map units.

1. Introduction

1.1. Background, study area, and previous work

The frequency and scale of landslides in a region are determined by external forcing and inherent, site-specific susceptibility. Tectonics and climate control the timing and location of landslides by setting the stage for slope instability through the creation of topographic relief via uplift and erosion (Montgomery and Brandon, 2002; Larsen and Montgomery, 2012) and providing landslide triggering mechanisms like earthquakes and rainfall (Keefer, 1984; Dai and Lee, 2001). However, the intact strength, geologic structure, and fracture density of the underlying bedrock govern whether a hillslope fails in a deep-seated landslide during a potential triggering event and control the landslide failure style

---

* Corresponding author.
E-mail address: seanlah@gmail.com (S.R. LaHusen).

https://doi.org/10.1016/j.enggeo.2023.107387
Received 22 May 2023; Received in revised form 12 December 2023; Accepted 16 December 2023

and kinematics. These material properties ultimately set the maximum relief of landscapes (Schmidt and Montgomery, 1995) and determine the scale and type of landslide hazards associated with them. Understanding the underlying susceptibility of a landscape to landslides is a critical need for reducing landslide-driven risk and losses, especially considering the potentially enormous impacts of large, deep-seated landslides. To account for the effect of lithology, landslide susceptibility models often rely on geologic maps as an input variable (Van Westen et al., 2008). These landslide susceptibility models can be statistical (e.g., García-Rodríguez et al., 2008; Lee et al., 2008; Nowicki Jessee et al., 2018; Reichenbach et al., 2018) or physics-based (e.g., Grant et al., 2016; Hess et al., 2017; Mathews et al., 2019) and have been widely used in landslide prone regions. Statistical models require knowledge of where hillslopes have failed in the past, relying on statistical methods including regression analysis to determine the importance of different landscape variables (surface slope, peak ground acceleration or velocity, lithology, etc.) derived from landslide inventories. Physics-based landslide susceptibility models require knowledge of bedrock frictional strength, cohesion, and density parameters that are often broadly generalized across a region, and for a limited number of rock types. Such models often rely on existing geologic maps and rarely account for variability within mapped geologic units, despite evidence that lithologic and structural differences have been shown to exert strong control on landslide occurrence (Guzzetti et al., 1996; Roering et al., 2005; Chen et al., 2011; Henriques et al., 2015; Perkins et al., 2017; Bhandari and Dhakal, 2018) and size (Valagussa et al., 2019). In many places this modeling simplification is not due to a lack of detailed geologic knowledge on the intra-unit variability of materials (e.g., variability in the Tyee Formation by Roering et al., 2005; or glacial sediments by Perkins et al., 2017), but rather stems from the convenience of using mapped geologic units for regional-scale landslide modeling. The conflation of mapped geologic units, which are often grouped by genetic history, and their geotechnical properties should be approached with caution as we demonstrate below.

To explore the effect of within-unit lithologic and structural variability on landslide susceptibility, we focus this study on the Eocene Tyee Formation in the central Oregon Coast Range (OCR), where widespread deep-seated bedrock landslides have been documented and studied for many decades (e.g., Baldwin, 1958; Roering et al., 2005; Burns, 2020; LaHusen et al., 2020; Struble et al., 2021). The Tyee Formation is composed of approximately 2 km of rhythmically alternating beds of sandstone and siltstone deposited as an Eocene submarine fan off the coast of present-day Oregon state in the Pacific Northwest United States (Diller, 1898; Snavely et al., 1964; Chan and Dott Jr, 1983; Santra et al., 2013). This fan has since been rotated 50°-70° clockwise such that the proximal fan facies underlie the southernmost portion of the mapped extent of the Tyee (Simpson and Cox, 1977). The proportion and bedding thickness of sandstone and siltstone varies, with lithological facies becoming generally more siltstone dominated in the more distal deposits to the north (Lovell, 1969; Chan and Dott Jr, 1983; Roering et al., 2005; Sweet et al., 2007). Despite having been uplifted from its original submarine position by at least two km to form the present-day OCR, most of the formation has been only minimally deformed into a series of broad, open folds, where dips rarely surpass 20 degrees (Vokes et al., 1951; Baldwin, 1955; Baldwin, 1961; Hoover, 1963; Snavely et al., 1972). Deep-seated landslides are ubiquitous in much of this region, and thousands of these landslides have been mapped in the last decade as the availability and quality of lidar data have dramatically improved our ability to identify and delineate large landslides under the characteristically dense forest canopy of the OCR (Burns, 2020; LaHusen et al., 2020).

The first comprehensive examination of the role of geologic structure and lithology in setting the stage for deep-seated failures in the OCR was published before lidar elevation data existed for the region. Roering et al. (2005) developed an automated landslide terrain identification tool which revealed widespread bench-like topography interpreted to be large deep-seated landslide deposits. Having identified these deposits, the authors pointed to a dramatic increase in landslide terrain from south to north, which they attributed to northward increasing siltstone content in the Tyee Formation. Further, they found the percentage of landslide prone terrain increases with dip angle, and this relationship is more pronounced in the silt-dominated facies of the northern Tyee. Comparisons between assumed landslide displacement vectors and bedding orientation led the authors to conclude that the vast majority of deep-seated landslides in the Tyee are structurally controlled and fail along weak siltstone beds.

This study tests the conclusions of Roering et al. (2005) and builds upon this foundational work in meaningful ways. We start by exploring how some of the most common drivers of landslides, and physical slope stability models (*Section 1.2*), fail to adequately explain the complex spatial patterns of landslides in the OCR. Rather than using an automated landslide detection tool with a coarse DEM, we rely on the manually mapped landslide inventory of LaHusen et al. (2020), which includes 9938 rotational and translational deep-seated bedrock landslide deposits mapped on 0.91-m resolution bare-earth lidar across 15,000 km^2 of the Tyee Formation of the central OCR. Each of these landslides has an estimated age of failure, derived from a calibrated surface roughness-age function, which opens the door for more accurate assessments of spatial and temporal patterns of deep-seated landsliding. The landslide inventory of LaHusen et al. (2020) was used to compute landslide areal densities throughout the Tyee, revealing a complex spatial pattern of landslides (Fig. 1, and *Section 2.2*). We add detailed rock mass characterization data (LaHusen and Grant, 2023) from bedrock outcrops in the field, then use a multivariable linear regression model to test for correlation between different geologic properties and deep-seated landslide density across space. Finally, we calculate the angular difference between each landslide in our study area and the orientation of the underlying bedrock to parse landslides into those that fail parallel to bedding (cataclinal landslides) and those that do not (non-cataclinal landslides).

1.2. Discordance in mapped landslides and physics-based stability models

To demonstrate the discordance between the measured areal density of deep-seated landslides and the modeled stability of deep-seated slip surfaces when homogenous geotechnical parameters are assumed, we use Scoops3D version 1.1 to calculate the lowest global factor of safety (FS) values for thousands of potential slip surfaces across two subsets of our study area. Scoops3D, a three-dimensional limit equilibrium model, is intentionally designed for deep-seated rotational failures, but is able to test thousands of potential spherical slip surfaces, such that the largest radius spherical surfaces come close to approximating translational or planar sliding (Reid et al., 2015). We assume the following geotechnical parameters, which fall within a reasonable range for sandstones: friction angle, 30°; cohesion, 500 kPa; and unit weight, 26 kN/m^3 (e.g. Wines and Lilly, 2003; Bandyopadhyay and Abdullah, 2013). Because recent studies have concluded that most of the deep-seated landslides in this region are triggered by rainfall rather than earthquakes (LaHusen et al., 2020; Grant et al., 2022), we use a ratio of pore-water pressure to vertical overburden stress (R_u) of 0.38, which approximates a fully-saturated scenario. Using these parameters, we run Scoops3D for two distinct 2 km^2 swaths of the study area: one characterized by widespread deep-seated landslides (high areal landslide density) and the other with only a single identifiable landslide (low areal landslide density).

Results from Scoops3D predict higher FS values in the areas of prolific landslides, and lower FS values in areas of few to no landslides (Fig. 1B – C). We tested different geotechnical parameters within a reasonable range and found that although the magnitude of FS across the landscape shifted, the spatial pattern did not, and changing these parameters did not change the generally discordant result between model output and mapped landslides. Alternative physics-based models, e.g., infinite slope stability for translational slides, also predict lower FS in

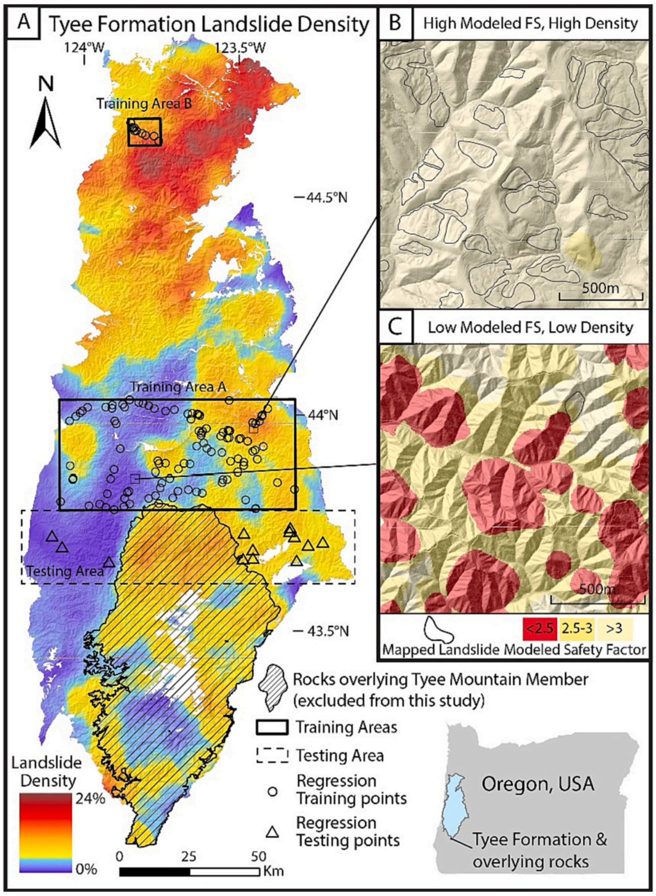

Fig. 1. Overview of deep-seated landslide patterns in the Tyee Formation of the Central OCR and selected slope stability modeling results using Scoops3D (Reid et al., 2015). Hillshade generated from lidar elevation data (Oregon Department of Geology and Mineral Industries). A. Landslide density across the Tyee Formation, measured as the percent of total area in a circular, 5-km radius moving window composed of landslide deposits from the manually mapped inventory of LaHusen et al. (2020). Rocks overlying the Tyee Mountain Member of the Tyee Fm. are not considered in this study (hatched pattern). Training Area A, Training Area B, and the Testing Area are outlined, with training points plotted as circles and testing points plotted as triangles. B. Bare-earth lidar hillshade of a selected region of high measured landslide density, colored by minimum FS (FS) calculated using Scoops3D (30° friction angle, 500 kPa cohesion, ru = 0.38), with mapped deep-seated landslides outlined in black. *C. bare*-earth lidar hillshade of region of low measured landslide density, colored by minimum FS calculated using Scoops3D (same model parameters as panel B), with a single mapped deep-seated landslide outlined in black.

regions with no deep-seated landslides, and high FS in regions with widespread landslides (see Fig. A2 in LaHusen, 2019). Overall, when homogenous rock strength parameters are assumed rather than accounting for variations in layered sedimentary rock, physical slope stability model results are inversely related to observed landslide density in our study area, suggesting the simplifying assumption of constant rock properties within the same geologic unit may be flawed.

Much of this discordance between modeled stability and mapped landslide locations can be attributed to the lack of correlation between landscape slope and landslide density (Fig. 2C). Slope is an important factor in all physics-based stability models, and higher slopes drive lower calculated FS values. This likely explains why such models fail to predict where deep-seated landslides are likely to occur in greater number. Studies of similar deep-seated landslides in New Zealand have also found enigmatic negative correlations between slope and landslide susceptibility, and these authors point to geologic structure and river incision as more important drivers of instability (Williams et al., 2021). Furthermore, in some portions of the OCR, deep-seated landslides are large and prolific enough that they measurably reduce mean hillslope gradients (Roering et al., 2005).

We also explored the correlation between landslide density and two major landslide triggers: earthquake strong ground motions and increases in pore-water pressure from rainfall. We find landslide density is negatively correlated with estimated ground shaking during past Cascadia Subduction Zone earthquakes from Wirth et al. (2021), which generally decreases with distance inland, away from the subduction megathrust fault (Fig. 2E). The relationship between rainfall and deep-seated landslides in the Tyee Formation is more complicated than that of slope or ground shaking. Although precipitation has been shown to be the dominant trigger for landslides that initiated here during the last 1000 years (LaHusen et al., 2020; Struble et al., 2021; Grant et al., 2022; Fig. 2B), there is no correlation between mean annual precipitation (MAP) and deep-seated landslide density over longer timescales ($R^2 = 0.00$), such as when all landslides in the mapped inventory are considered (Fig. 2D). This type of split-timescale analysis is possible using the roughness-age estimates in the landslide inventory. Although some of this discordance between the recent (1000 yr) and longer timescale landslide records could be due to changing spatial patterns of precipitation, we propose that variability in the inherent susceptibility within the same mapped geologic formation must exert some control on landslide density. In this study, we define inherent susceptibility as the propensity for a slope to fail in a deep-seated landslide during a triggering event, controlled by the physical properties of the underlying bedrock. Theoretically, if the entire study area was impacted by the same precipitation intensity and duration during a prolonged winter rainstorm or experienced the same strong ground motions during an earthquake, sites with higher inherent susceptibility would be most likely to fail. Rather than aim to develop a comprehensive model to predict landslide likelihood, we instead use a multivariable linear regression (MVR) model to determine how much of the spatial variability in deep-seated landslide occurrence is controlled by lithological and structural variability within the same mapped geologic unit.

2. Methods

2.1. Field observations and data collection

To examine the effects of local lithological and structural bedrock variability on landslide susceptibility, we collected rock mass and structural data from 128 bedrock outcrop sites within the Tyee Mountain Member of the Tyee Formation (Baldwin, 1974; Fig. 1; Fig. 3). In order to ensure an appropriate spatial density of points, we selected three areas to focus our data collection within the geographically expansive Tyee Formation: 105 sites from a large 40 × 80- km rectangular swath which spans the width of the central OCR (Training Area A in Fig. 1), 10 sites from a smaller 10 × 11-km swath ~100 km to the north of Training Area A (Training Area B in Fig. 1), and 13 sites from a separate area south of and adjacent to Training Area A where points were used only during the testing and validation steps of our analysis (Testing Area in Fig. 1). Field observations were primarily focused within the larger Training Area A to maximize dense data collection at locations accessible from the road network that spanned a wide range of observed landslide densities. The smaller Training Area B to the north was included because it captures some of the highest landslide densities observed in the Tyee Formation and represents a distal and finer-grained portion of the ancient submarine fan (Roering et al., 2005). Training Area B also takes advantage of excellent roadcut outcrops along a newly re-routed section of Oregon's Highway 20, which is particularly prone to deep-seated landslides (Hammond et al., 2009). With the exception of some roughly *E*-W trending volcanic dikes (Vokes et al., 1951; Struble and Roering, 2021a) both training areas are exclusively underlain by the Tyee Mountain Member of the Tyee Formation. The Testing Area, located directly south of Training Area A, also includes portions of the

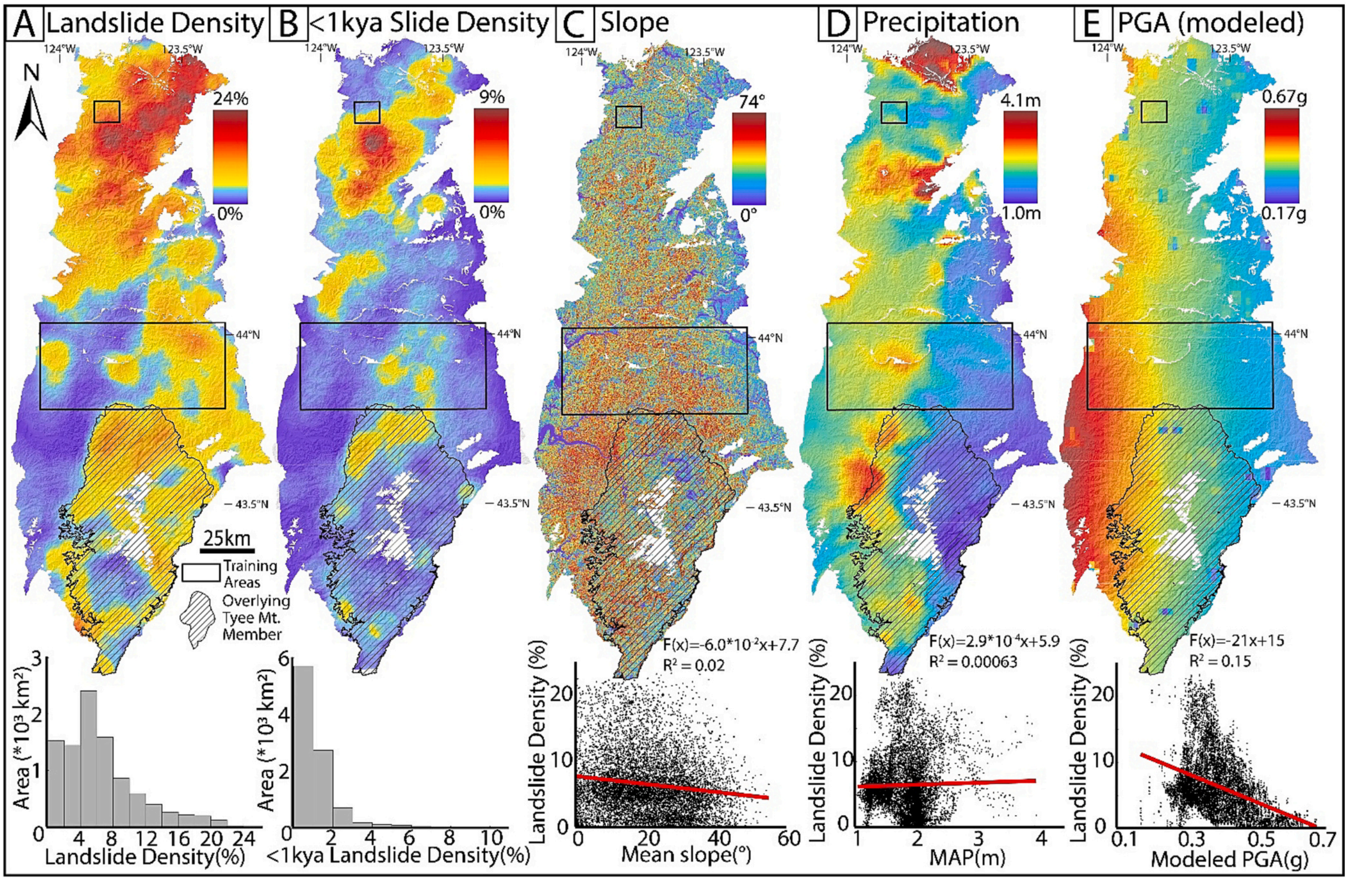

Fig. 2. A. Map of landslide areal density (calculated as the percentage of landslide terrain within a 5-km radius moving window) within the Eocene Tyee Mountain (Mt.) Member of the Tyee Formation and for overlying members of the Tyee Formation (hatched pattern). Corresponding histogram shows distribution of landslide density values. B. Map of areal density of only recent landslides estimated to be <1000 years old using surface roughness dating. C. Landscape slope (calculated as the mean slope within a 2-km diameter moving window after excluding cells <5°) and a corresponding plot of slope vs. landslide areal density, with best fit linear regression shown in red. D. Mean annual precipitation (PRISM Climate Group, 2019), averaged over a 30 year span ending in 2018) and a corresponding plot of precipitation vs. landslide areal density, with best fit linear regression shown in red. E. Modeled peak ground acceleration during a magnitude 9.0 Cascadia Subduction Zone earthquake (we use the mean of dozens of synthetic earthquake scenarios from Wirth et al. (2021)) and a corresponding plot of modeled PGA vs. landslide areal density, with best fit linear regression shown in red. (For interpretation of the references to colour in this figure legend, the reader is referred to the web version of this article.)

Baughman and Elkton Siltstone Members of the Tyee Formation (Baldwin, 1974; Madin, 2016), rocks that are overlying the Tyee Mountain Member of the Tyee Formation, though these members are not considered in this study. The overlying Elkton Siltstone Member of the Tyee, does not uniformly exhibit the alternating pattern of rhythmically bedded sandstone and siltstone beds like the Tyee Mountain Member. To further constrain our study to the effects of variability within the Tyee Formation, and specifically the Tyee Mountain Member, we omit regions of the Testing Area with surficial overlying Elkton Siltstone and Baughman Members.

Prior work suggests the ratio of fine-grained beds to coarse-grained beds exerts strong control on landslide susceptibility in the Tyee (Roering et al., 2005) and elsewhere (Schmidt and Montgomery, 1996; Henriques et al., 2015; Perkins et al., 2017) so we collected a set of measurements specific to rhythmically-bedded sedimentary rock rather than adopt more generalized rock mass characterization techniques such as geological strength index (GSI), rock mass rating (RMR), rock mass quality (RMQ), or rock mass strength (RMS). We selected sites where at least 2 m of stratigraphic section was exposed and prioritized sites with >10 m of exposed, unweathered stratigraphic section, relying primarily on roadcuts which are ubiquitous in the OCR due to a vast network of past and present logging roads. We assume that the lithologic characteristics of these bedrock outcrops are representative of the immediate vicinity as well as the subsurface, where landslide slip surfaces may form. The most extensive outcrops included in this study, with bedrock exposures of >20 m tall and hundreds of meters wide, showed no evidence of substantial variability, suggesting assumptions of local similarity in lithological characteristics are reasonable.

At each outcrop site, we recorded the proportion of siltstone to sandstone measured in the total exposed section, the maximum thickness of the sandstone and siltstone beds, the strike and dip of bedding, and Schmidt Hammer rebound values for sandstone beds which provide an estimated proxy for uniaxial compressive strength (Aydin and Basu, 2005). Although shear strength along a slip surface is more directly related to slope stability, we use compressive strength in this study because it can be readily estimated in-situ using the Schmidt Hammer with no need for geotechnical lab testing, is related to shear strength and can be used in conjunction with GSI to estimate cohesion and friction angle if desired (Hoek et al., 2002), and provides an indirect measure of the induration of the sandstone beds. Schmidt Hammer measurements were used as a proxy for intact sandstone strength, but we acknowledge the likely effect of surficial weathering on our measured values (Retallack and Roering, 2012), even at bedrock sites only recently (tens of years) exposed in roadcuts (Stock et al., 2005), as a source of uncertainty.

We focus on the properties and orientation of stratigraphic bedding rather than other discontinuities like fractures because we observe a low density of fractures outside of bedding, and very few regularly oriented

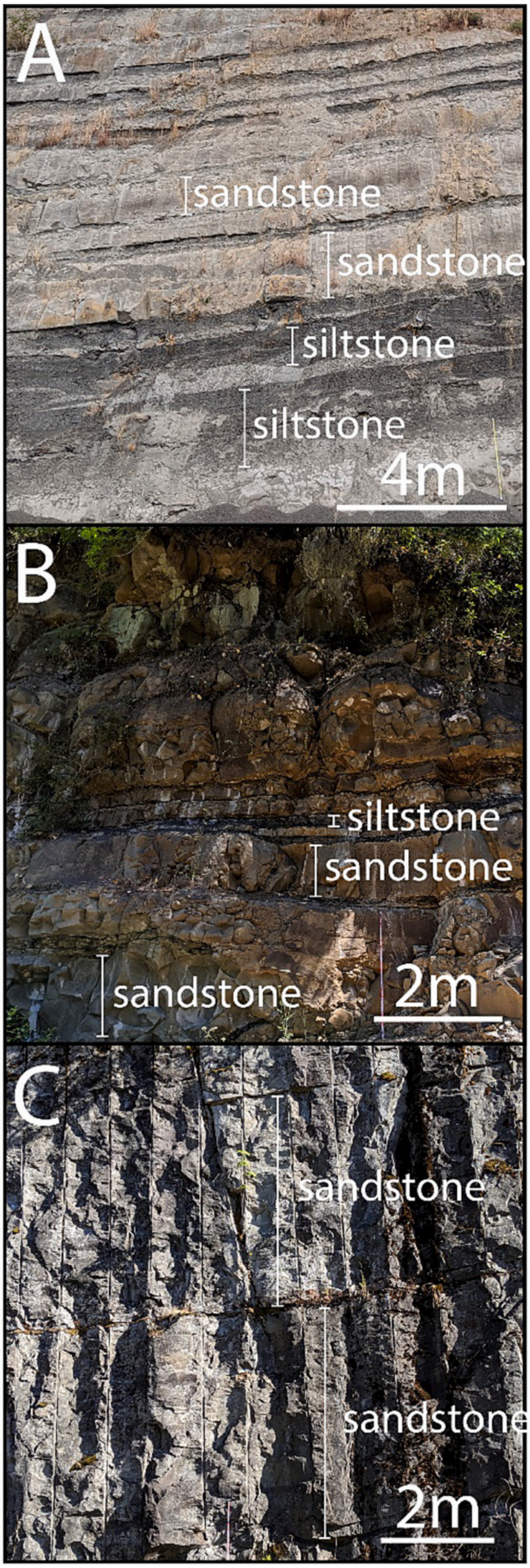

Fig. 3. Photos of three field sites showing variability in thickness and proportions of sandstone and siltstone beds. Select sandstone and siltstone beds are outlined using brackets. A. Site 'Tyee_0821_3' is characterized by relatively high siltstone content (50%), which appears as darker beds, B. Site 'Tyee_0714_6' has a moderate proportion of siltstone (15–20%), C. Site 'Tyee_0714_15' is massive sandstone (~1% siltstone), with individual sandstone beds up to 5-m thick. Photographs by Sean LaHusen, U.S. Geological Survey, 2020.

joint sets, although bedding forms a prominent discontinuity at all outcrops. To minimize error from single point measurements of bedding attitudes in gently dipping rock with sometimes wavy bedding contacts, we combined our own bedding attitude measurements (LaHusen and Grant, 2023) with 843 strike and dip points digitized from geologic maps (Vokes et al., 1951; Baldwin, 1955; Baldwin, 1961; Snavely et al., 1972), which we used to create an interpolated surface of bedrock strike and dip. Additional details on this interpolation are provided in *Section 2.3*.

2.2. *Modeling inherent landslide susceptibility using multivariable linear regression*

To correlate these variables to inherent landslide susceptibility, we assume that landslide areal density correlates to inherent susceptibility. Although significant landslide triggering events like great earthquakes or major atmospheric rivers may have signals imbedded in the landslides of the Tyee Formation, we assume the lack of correlation between precipitation, earthquake shaking, and slope (Fig. 2) implies much of the landslide density pattern in the Tyee Formation is driven primarily by variability in the inherent susceptibility of the bedrock. Although landslide number-density would reveal more about discrete landslide events and triggering, we chose to use areal density to reflect the underlying susceptibility more accurately, because larger, continuous regions of high susceptibility may be conducive to larger landslides. For this study, we calculated landslide density as the percent of area within a 5-km radius moving circular window composed by deep-seated landslide deposits, using the LaHusen et al. (2020) inventory of 9938 landslides. We tested moving window radii from 3 to 9 km, and found that, while the coefficient of determination (R^2) for our MVR model slightly increased with expanding window size, window sizes larger than 5 km failed to sufficiently capture the complex nature of changing landslide susceptibility across the study areas (SM Fig. 1). This loss of spatial information with larger window sizes is expected, because as window sizes get larger, the variance in landslide density decreases by effectively smearing the high-density zones into the low-density zones. A large enough window size would simply capture the entire study area in a single window and yield the mean value of landslide density across the study area. Meanwhile, smaller window sizes were not appropriate for the scale of landforms considered in this study, where individual landslide deposits are up to 2 km long in one dimension. Moreover, the furthest distance between our field measurement points is 10 km, so choosing a moving window of 5-km radius ensured that our moving windows should contain multiple field sites.

Following data collection, we examined correlation plots between variable pairs to test for correlation between predictor variables and landslide areal density and collinearity amongst predictor variables for all data collected at the 115 sites within the training areas (SM Fig. 2). These plots and statistical tests helped with variable selection for the MVR model. For each variable pair, we calculated the correlation coefficient (r) and p-value to gauge the strength and statistical significance of a linear relationship between the variables. We adopted the conventional p-value threshold of <0.05 as the p-value that signifies a statistically significant linear relationship. Variable pairs with $p < 0.05$ reject the null hypothesis that there is no linear correlation between variables, so we consider these variable pairs to have a statistically significant linear correlation. We exclude any predictor variables that do not have a statistically significant correlation with landslide density, our independent variable. To limit the effects of collinearity amongst predictor variables, if two predictor variables showed a statistically significant monotonic relationship, the variable with the weaker correlation with landslide density was not considered in the MVR model. After excluding collinear predictor variables, we selected all predictor variables with statistically significant linear correlations with landslide density as inputs to our MVR model.

We assessed our model performance in three ways. First, we calculated standard statistical measures of R^2 and p-value for the entire MVR model. R^2 describes the proportion of variance in landslide density explained by the MVR model, whereas the p-value tests whether the model is statistically significant. Second, we visually inspected the predicted landslide density from the model in map view and compared this predicted density with the measured density to examine model performance across space. To construct a continuous 2D MVR output, we interpolate each predictor variable via Kriging in ArcGIS Pro (v3.1.1, Esri) from measured values within Training Area A (Fig. 4). We focus these variable interpolations on Training Area A alone because Training Area A is larger and contains far more field sites (105 of 115 total sites) than Training Area B, and the distance between the two sites precludes reasonable interpolation. We tested both Simple and Ordinary Kriging interpolation methods and selected the model that provided the lowest absolute error for each variable. Ordinary Kriging, with no data transformation, was used for all variables except Bedding Dip, for which Simple Kriging yielded better fit. During this step, dip direction was decomposed into northing and easting components, which were independently interpolated via Simple Kriging. Each of the 2D predictor variable interpolations were then used as an input for a 2D MVR model raster, which we compared to measured landslide density to evaluate the accuracy of spatial trends and identify locations where the model over or under-predicted landslide density (Fig. 5). We subtract the measured landslide density from our MVR-predicted landslide density to make an error map which highlights where our model overestimates or underestimates actual landslide density (Fig. 5). Third, we evaluated model performance by testing the model's ability to predict landslide density at 13 sites in the separate Testing Area. We calculated the prediction error at each test point by taking the difference between the model-predicted landslide density and the measured landslide density. More qualitatively, we also assessed the ability of the model to correctly predict spatial patterns in landslide density.

2.3. Landslide failure style from 2D geologic structure interpolation

Detailed geologic information can also be used to assess structural controls on landslide failure mechanics. Alignment of surface slope relative to underlying bedding can be a strong predictor of deep-seated landslides because weak beds can act as slip surfaces for translational bedrock landslides (Schmidt and Montgomery, 1996; Guzzetti et al.,

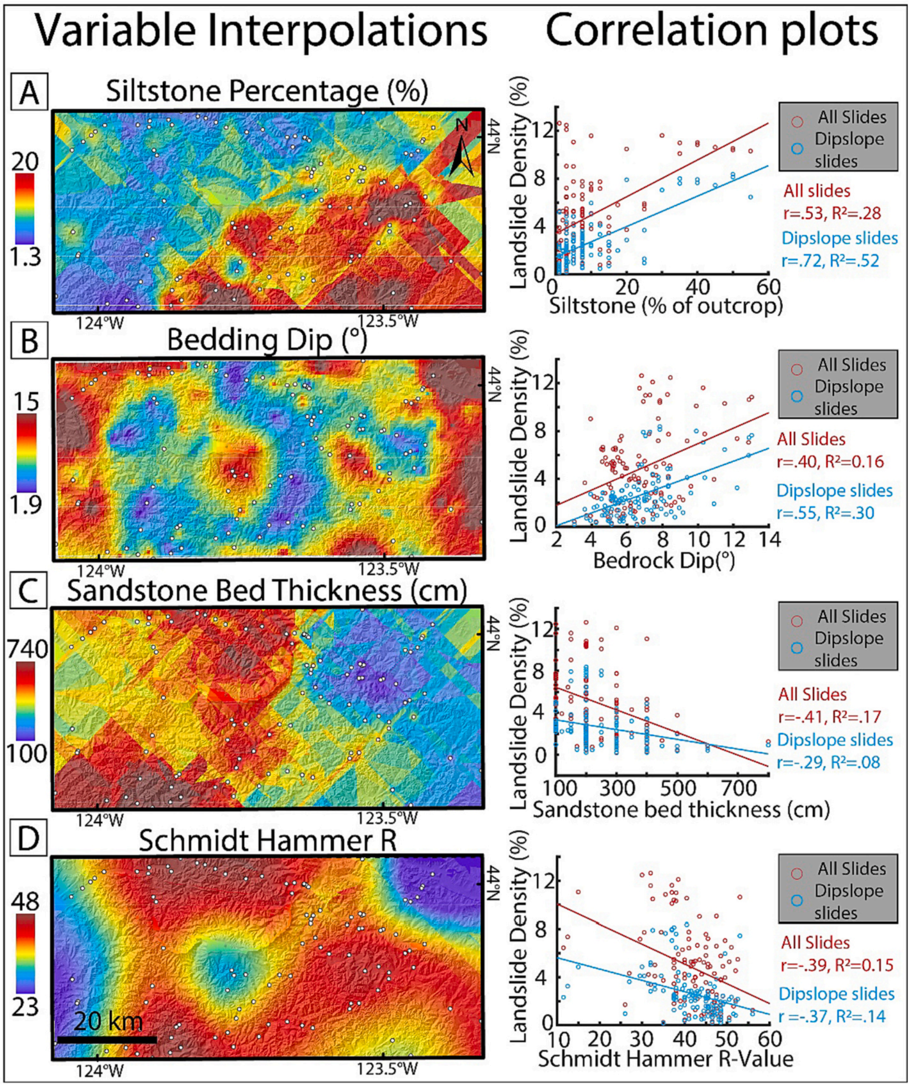

Fig. 4. Interpolated maps and plots of each predictor variable against landslide density: A. Siltstone percentage, B. Bedding dip, C. Sandstone max bedding thickness, and D. Schmidt Hammer R. Maps of each predictor variable are interpolated across Training Area A using Ordinary Kriging. To the right of each interpolation, the predictor variable value at each observation site is plotted against areal density of all landslides (red) and areal density of just cataclinal (bedding-parallel) landslides (blue). Best-fit linear regressions and corresponding r and R^2 values are reported. Interpolated maps of each predictor variable are used in the MVR model across the larger study area. (For interpretation of the references to colour in this figure legend, the reader is referred to the web version of this article.)

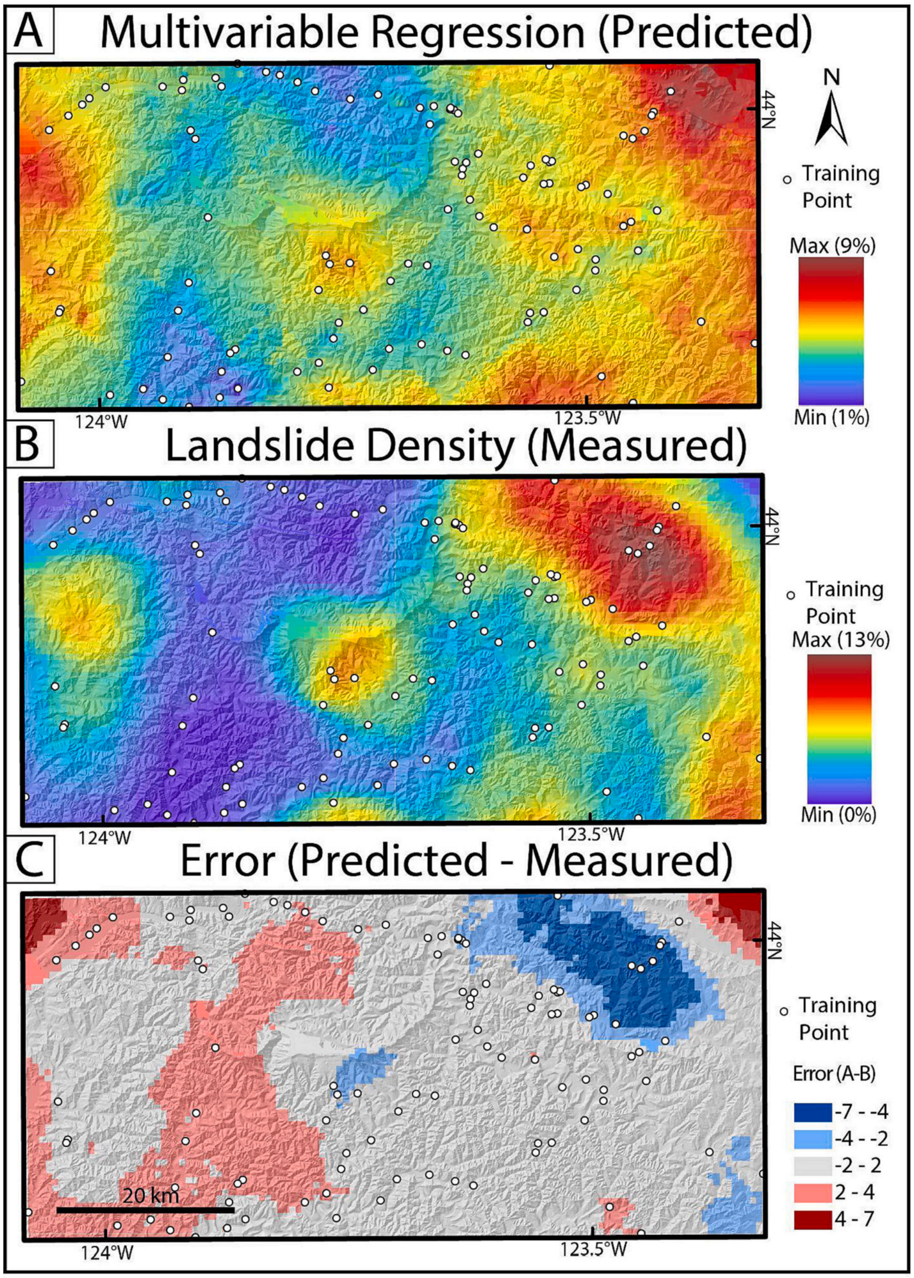

Fig. 5. Linear multivariable regression model results: (A), measured landslide density (B), and error between model prediction and measured density (C) in Training Area A (limits shown in Fig. 1). On all maps, training points in area A are shown as white circles.

1996; Williams et al., 2021). Roering et al. (2005) demonstrated how the gentle folds of the Tyee Formation controlled landslide failure direction by revealing the propensity for bench-like landslide terrain to form on cataclinal hillslopes, where the landscape slope gradient parallels bedding dip direction. To expand on the kinematic findings of Roering et al. (2005), we developed a continuous model of bedding dip direction and magnitude within the Tyee Formation to compare against the mapped landslide inventory of LaHusen et al. (2020).

Dip direction and magnitude were interpolated using Kriging (*Section 2.2*) from a compilation of 971 bedding attitude measurements across a continuous swath encompassing both Training Area A and the Test Area. Because no regression models in this study use bedding attitude data, we combined Training Area A and the Test Area into a single Kriging interpolation to better leverage the available data. Like before, Training Area B was intentionally excluded from this interpolation because it is geographically distant from training area A and the Testing Area (Fig. 1). We digitized 843 strike and dip measurements from multiple geologic maps (Vokes et al., 1951; Baldwin, 1955; Baldwin, 1961; Snavely et al., 1972) to supplement our field observations (LaHusen and Grant, 2023) and greatly improve the resolution of our interpolated bedding attitude estimates. Minimal faulting, the long-wavelength nature of folding, and a high density of existing bedding attitude data from regional geologic maps and new data points from this study allowed us to create detailed interpolated maps of dip direction and magnitude. Although this method may be inappropriate for places underlain by more highly deformed bedrock, we argue that it is a powerful tool to construct relatively accurate, continuous interpolations of geologic structure in modestly deformed rocks like the Tyee Formation. Previous workers used remotely mapped bedding orientations to construct similar interpolations, which underscores the importance of the interaction between bedrock and landscape orientation in controlling deep-seated bedrock instabilities (Santangelo et al., 2015).

To better understand the role of geologic structure in deep-seated landslide formation, we compared underlying geologic structure with landslide orientations. To do this, we calculated the mean aspect for each of the 3096 mapped deep-seated landslide deposits within the structural interpolation area. We assume that the present-day landslide deposit aspect is roughly parallel to the landslide slip surface aspect, and therefore reflects the direction of landslide displacement. To calculate mean landslide aspect, we performed the same steps as with bedding: first parsing each DEM cell contained within a landslide deposit into its northing and easting components, then using the average northing and easting value in each landslide polygon to calculate mean aspect for the entire deposit. Although surficial features like gullies and hummocks may add noise to this mean aspect calculation, we assume that, given the large size of landslide deposits considered here, these features do not systematically bias the mean aspect calculation. The difference between landslide aspect and underlying bedding dip direction (rake) was then calculated for each landslide in the inventory. We assume computed rake angles represent the map-view angle between slide displacement direction and bedding dip direction. A rake value of 0° would imply landslide displacement parallel to bedding (cataclinal), with 90° rake reflecting displacement perpendicular to bedding dip direction, and 180° perfectly anaclinal landslide displacement opposite of bedding dip direction. For this study, we define a threshold rake value of 45° below which landslides are deemed cataclinal and above which they are considered non-cataclinal failures. We assume cataclinal landslides are most often structurally controlled, translational bedrock landslides failing at least partially along a slip surface parallel to bedding, whereas non-cataclinal slides (including but not limited to landslides on anaclinal slopes) have subsurface geometries that are unlikely to be influenced by the orientation of bedding, and may be more likely to be rotational in style. Although 45° is an arbitrary cutoff, it means that the landslide slip direction and bedding dip direction lie within a 90° quadrant window. Parsing the landslide inventory into cataclinal and non-cataclinal failures allows landslide density to be calculated separately for both of these implied failure styles. We then repeat the MVR analysis (*Section 2.2*) for both cataclinal and non-cataclinal landslide density layers to test whether landslide failure style affects the relative importance of each of the geologic predictor variables we measured in the field.

3. Results

3.1. Multivariable regression model and performance

Using the LaHusen et al. (2020) deep-seated landslide inventory, we found areal landslide density is highly variable across the Tyee Formation, ranging from 0 to 24% (Fig. 1A). As in Roering et al. (2005), we observe a general northward increase in landslide density. However, this analysis also highlights additional complexity in the spatial patterns of landslides not explained by a simple 1-dimensional south to north gradient (Fig. 1). For example, there is little existing evidence to explain the observed heterogeneity in east-west landslide density across the Tyee Formation (Heller and Dickinson, 1985; Roering et al., 2005).

Stratigraphic and structural measurements were collected at 115 training points and 13 testing points, which collectively represent the variability of bedrock characteristics that define the Tyee Formation (Fig. 3; see also SM Table 1 and LaHusen and Grant, 2023). Landslide density sampled at all 115 training points varies from 0.22%–13%. The proportion of siltstone ranges from 1% to 55% with a mean of 9.3%, sandstone bedding maximum thickness ranges from 100 cm – 800 cm with a mean of 250 cm, siltstone bedding maximum thickness ranges from 0 cm – 250 cm with a mean of 26 cm, Schmidt Hammer R-value (S_r), calculated as a mean of 10 point measurements on sandstone facies only, ranges from 12 to 56 with a mean of 42, and interpolated bedrock dip at each point ranges from 3° – 13°. S_r values for siltstone facies were attempted at several locations but the siltstone was extremely friable and below the sensitivity of the Schmidt Hammer used in this study. We instead assume siltstone represents a substantially weaker lithology than sandstone across the study area but do not report quantitative strength estimates.

While collecting Schmidt Hammer measurements, we omitted any strikes that sounded atypically hollow or where a rock fragment visibly broke, as these strikes were often associated with surficial fractures. We did observe signs of physical weathering on many sandstone surfaces throughout the study area, including surface parallel fractures and surficial crumbling and sandy coatings, so we intentionally targeted less weathered surfaces where possible. Specifically, we tried to measure dry faces without signs of near-surface fractures or faces where the fractured outer layer appeared to have spalled off the surface, revealing relatively unfractured intact sandstone beneath (SM Fig. 3). Inclement weather meant that some locations were measured when wet. For most sites, the low standard deviation in S_r (average SD = 4.2, SM Table 1; LaHusen and Grant, 2023) suggests we were able to target mostly uniform intact rock for Schmidt Hammer strikes. At 4 sites, we observed universally high surficial weathering, and we could not avoid measuring these crumbling surfaces (See 'notes' column in SM Table 1; LaHusen and Grant, 2023). However, we posit that outcrops with lower intact strength may also weather more rapidly (e.g. a poorly-cemented sandstone may fracture or disintegrate into sand more rapidly than a well-indurated and strongly-cemented sandstone), such that surficial weathering may be somewhat reflective of intact strength. Still, the weathering process likely introduces uncertainty to a variable that would ideally be measured on totally fresh surfaces.

Table 1

Results table for three multivariable linear regression analyses: All Landslide Density (blue), Cataclinal Landslide Density (green), and Non-cataclinal Landslide Density (yellow). For each predictor variable (P_{silt}: percentage siltstone, T_{sand}: max sandstone bedding thickness, S_R: mean Schmidt Hammer R-value as defined in Eq. (1)), *p*-values and correlation coefficient (r) describe the linear relationship between the predictor variable and each independent variable (landslide density). If the predictor variable passes the p-test to be included in the MVR regression, its coefficient in the MVR model is also listed. Variables not used in a model are white (not colored). Statistics that describe the goodness of fit for each multivariable regression - error variance, p-value, and R^2 - are also listed.

Independent Variable	Predictor Variable Statistics												MVR results			
	P_{silt}			T_{sand}			S_R			Dip						
	MVR coef b	p-value	r	MVR coef b	p-value	r	MVR coef b	p-value	r	MVR coef b	p-value	r	Intercept	Error Variance	p-value	R^2
All Landslide Density (%)	1.11E-01	8.8E-10	0.53	-9.81E-02	4.6E-06	-0.41	-6.65E-03	1.5E-05	-0.39	2.79E-01	9.6E-06	0.40	7.7	5.7	1.9E-14	0.47
Cataclinal Landslide Density (%)	1.02E-01	5.2E-20	0.72	-1.44E-03	1.5E-03	-0.29	-5.26E-02	4.7E-05	-0.37	2.61E-01	1.9E-10	0.55	2.5	1.3	1.1E-25	0.67
Non-cataclinal Landslide Density (%)	Not used	6.0E-02	0.18	-5.58E-03	2.7E-06	-0.42	-5.54E-02	5.0E-04	-0.32	Not used	2.8E-01	0.10	5.7	5.8	6.5E-07	0.22

All of the variables measured in the field show a statistically significant linear correlation with areal landslide density (p-value <0.05). Siltstone percentage, siltstone maximum bed thickness, and bedding dip magnitude are all positively correlated to landslide density with correlation coefficients (r) of 0.53, 0.48, and 0.40, respectively, whereas sandstone bedding thickness and S_r are both negatively correlated with landslide density with correlation coefficients of -0.41 and -0.39, respectively (Fig. 4, and SM Fig. 2). During model selection, we tested for covariance and interaction between predictor variables to remove strongly collinear inputs and improve model performance. We removed siltstone maximum thickness from the MVR model because it is highly collinear with siltstone percentage ($r = 0.92$) and showed less single-variate correlation to landslide density. The only notable interaction term was sandstone maximum bed thickness in cm (T_{sand}) and sandstone facies compressive strength (S_r), i.e., $T_{sand} * S_r$, $r = -0.47$, but this variable was not included because it did not improve overall model performance. We use each of these remaining predictor variables to calculate a best-fit multivariable linear regression to landslide density:

$$\rho_{LS} = 7.7 + \left(1.11*10^{-1}\right)P_{silt} - \left(9.81*10^{-2}\right)T_{sand} - \left(6.65*10^{-3}\right)S_r + \left(2.79*10^{-1}\right)Dip \tag{1}$$

Where: ρ_{LS} is the density of deep-seated landslide calculated as a percent of total area within a 5-km radius moving window, P_{silt} is the percentage of siltstone facies beds of the total exposed outcrop, Dip is the magnitude of bedding dip, in degrees, and T_{sand} and S_r are defined above.

With an R^2 value of 0.47 and a p-value of $1.9*10^{-14}$, this model for landslide density is statistically significant and explains nearly half of the measured variance in landslide density within our 115 training points (Table 1). Our spatially continuous model results, calculated using interpolated variable maps, shows model prediction is within 2% of the measured density for much of the study area (Fig. 5). However, this analysis highlights a large swath of modest overestimation in the central portion of the training area (2–4% absolute error), and a roughly circular zone of substantial underestimation in the NE quadrant of the training area with >4% absolute error (Fig. 5C). Other smaller zones of high error are found in the extreme corners of Training Area A are likely a product of edge effects during interpolation of input data and the lack of observation sites to accurately interpolate at those extremes.

The Testing Area shows a pronounced trend in landslide density - with the east side of the area characterized by much higher landslide density than the west, making it ideal to assess the ability of the MVR model to correctly predict spatial patterns (Fig. 6). When applied to the Testing Area, predicted landslide density values range from 0.20% to 7.8%, compared to a measured range of 0.94% to 12%. Overall, our predicted values have a smaller range and tend to overestimate the measured density by 1.6%, with a standard error of 2.4%, and a maximum error of 6.7% at a single point (Fig. 6). The MVR model correctly identifies the overall spatial pattern of observed landslides across the Test Area, predicting lower deep-seated landslide susceptibility in the west, and higher susceptibility in the east (Fig. 6).

3.2. *Evaluating structural controls on landslide style*

By assuming the landslide deposit orientations approximate the slip surface beneath, we examine trends in landslide directionality and compare landslide slip surface orientation with underlying bedding orientation to test for structural control on landslide failure style (Fig. 7). Plotting landslide orientations and bedding orientations (for each cell in the interpolated bedding dip direction raster) on a rose diagram for comparison reveals a strong bimodal trend in bedding attitude (Fig. 8A). Two general bedding orientations underlie much of the study area: S through WNW facing beds (180° –300°) and ENE through SE facing beds (60° – 120°), which align with the many broad, southward-plunging fold hinges mapped in the study area. Landslides follow a similar, but slightly less bimodal azimuthal distribution to bedding, with the highest proportion of landslides occurring on southwest aspects.

We identify 1734 cataclinal landslides (rake <45°) with a total deposit area of 91.7 km^2, representing just over half (56%) of the total number of landslides and 63% of the total landslide area within the bedding interpolation (Fig. 7). Non-displope failures comprise 1362 landslides but just 37% of the total landslide area, due to the smaller average size of non-cataclinal landslide deposits: 39,500 m^2 vs. 52,900 m^2 for cataclinal landslide deposits. Though they represent a minority of landslides in the study area, the proportion of non-cataclinal slides is not insignificant and was previously unrecognized (Roering et al., 2005). Having parsed the landslide inventory by cataclinal and non-cataclinal landslides, we calculate new MVR models specific to these distinct landslide sets (Table 1). This exercise illuminates the disparity in the ability of our stratigraphic and structural input variables to predict cataclinal slides versus non-cataclinal slides. Our regression performance improves dramatically for cataclinal failure density, compared with the regression for all landslides - resulting in an R^2 value of 0.67 and a p-value of $1.1*10^{-25}$. However, when we regressed the same variables to non-cataclinal failure density, the resulting correlation was quite poor, with an R^2 value of just 0.22. Moreover, while all of the predictor variables show a statistically significant correlation with cataclinal landslide density, only sandstone maximum thickness and Schmidt hammer R-value were correlated with non-cataclinal density. Siltstone percent, the variable with the strongest correlation with all landslide density and cataclinal landslide density, was only weakly

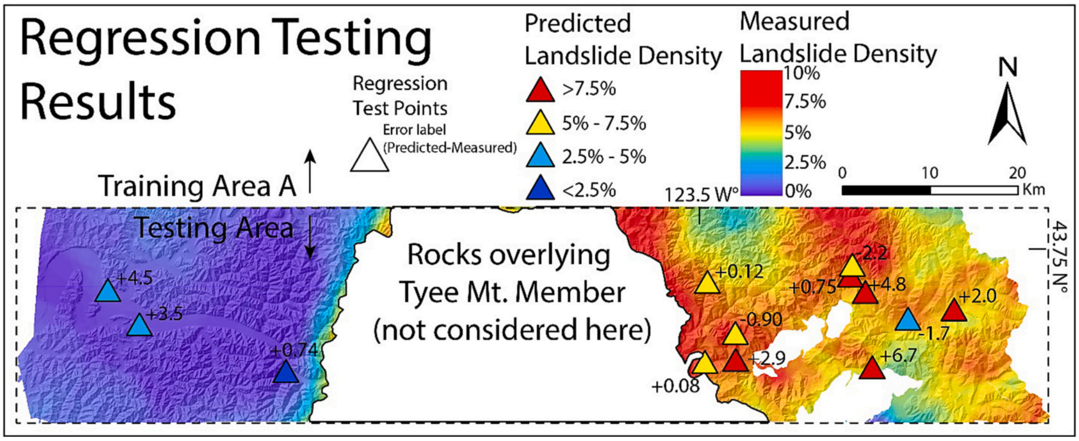

Fig. 6. Map of the regression Testing Area (limits shown on Fig. 1), comparing measured landslide density with predicted landslide density. Map is colored by measured landslide density, and test points are plotted as triangles colored by predicted landslide density using the multivariable regression which was developed in the training areas using a separate set of points. Error, calculated as the predicted density minus the measured density, is labeled at each point.

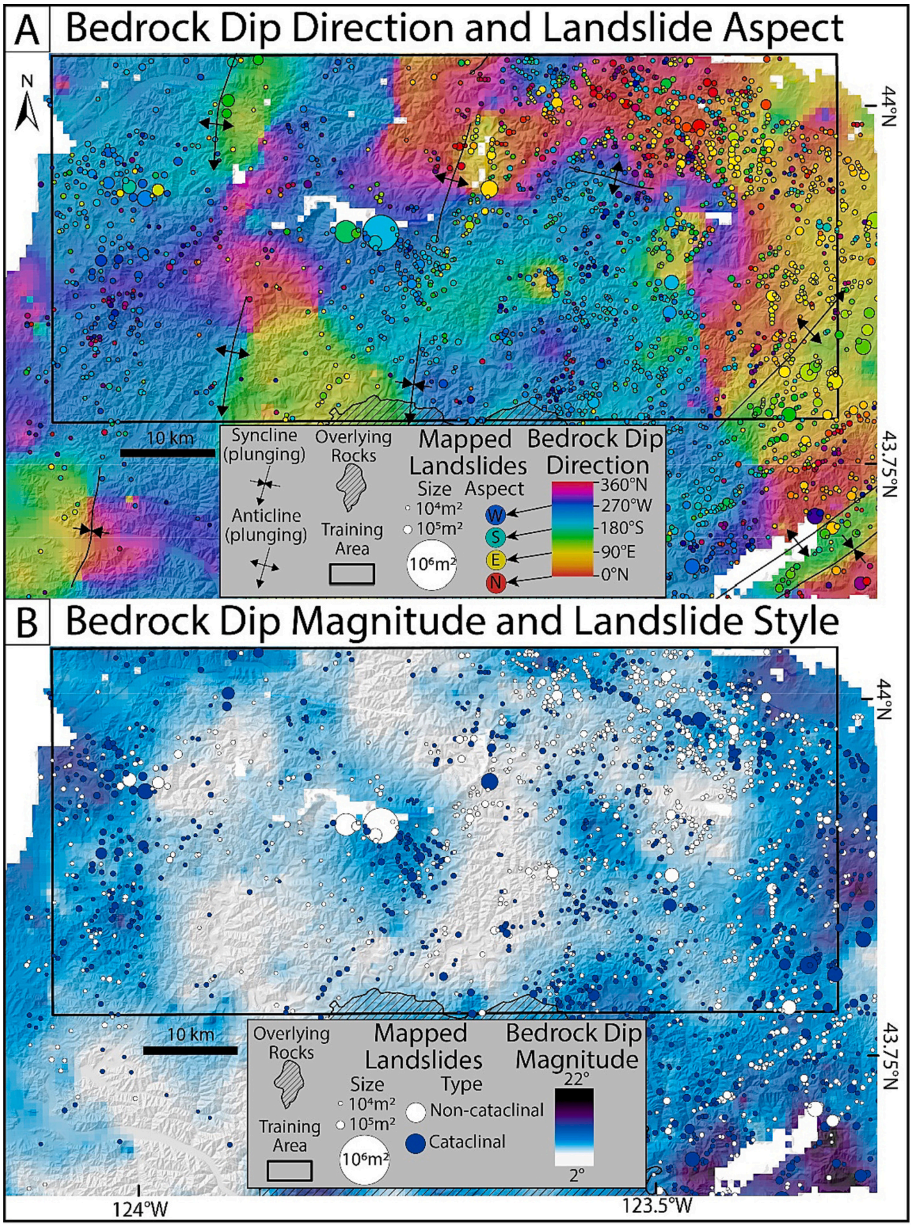

Fig. 7. A. Map comparing underlying bedrock dip direction with landslide aspect. Basemap colored by interpolated bedrock dip direction from 971 strike and dip measurements (LaHusen and Grant, 2023; Vokes et al., 1951; Baldwin, 1955; Baldwin, 1961; Snavely et al., 1972). Deep-seated landslides are shown as circles, scaled by landslide deposit area, and colored by landslide aspect using the same colour bar symbology as bedrock dip direction. Where landslide colors are similar to map colour, landslides are failing parallel to bedrock dip direction. B. Map comparing bedrock dip magnitude with landslide failure style. Landslides shown as circles, scaled by area, and colored by type: cataclinal failures (blue) and non-cataclinal failures (white). (For interpretation of the references to colour in this figure legend, the reader is referred to the web version of this article.)

correlated with non-cataclinal density and is not significant (p-value >0.05, Table 1).

Although bedding dip is quite shallow throughout the testing and training areas (95% of the bedding measurements are <17° and the interpolation never exceeds 20°), there is a strong correlation between dip magnitude and landslide rake (Fig. 8B). After binning mapped landslides into 2° dip magnitude bins, we plot dip against average landslide rake per bin. Because the maximum theoretical rake value is 180°, a mean of 90° would suggest totally random landslide orientations relative to bedding, and 0° would suggest a preferential landslide orientation parallel to that of the underlying bedrock structure. A strong negative correlation exists between dip magnitude and landslide rake (Fig. 8B). At dips below 7° - 9°, the average landslide rake exceeds 60°, while landslide rake drops to 20°- 40° at dips above 13°.

4. Discussion

4.1. *MVR model nuances and the importance of intra-unit variability*

Our MVR model explains nearly half of the variability in deep-seated landslide density across the training areas ($R^2 = 0.47$) and accurately predicts regional patterns in landslide density within the separate Testing Area, despite some relatively high errors at individual test points. This model is not meant to be a comprehensive landslide hazard model, but rather a test of the relative influence of structural and stratigraphic bedrock properties on the inherent susceptibility to deep-seated landslides across space in a particularly enigmatic region. Only simplified geologic factors are considered in this analysis (structure, lithology, and an estimate of intact compressive strength). Although

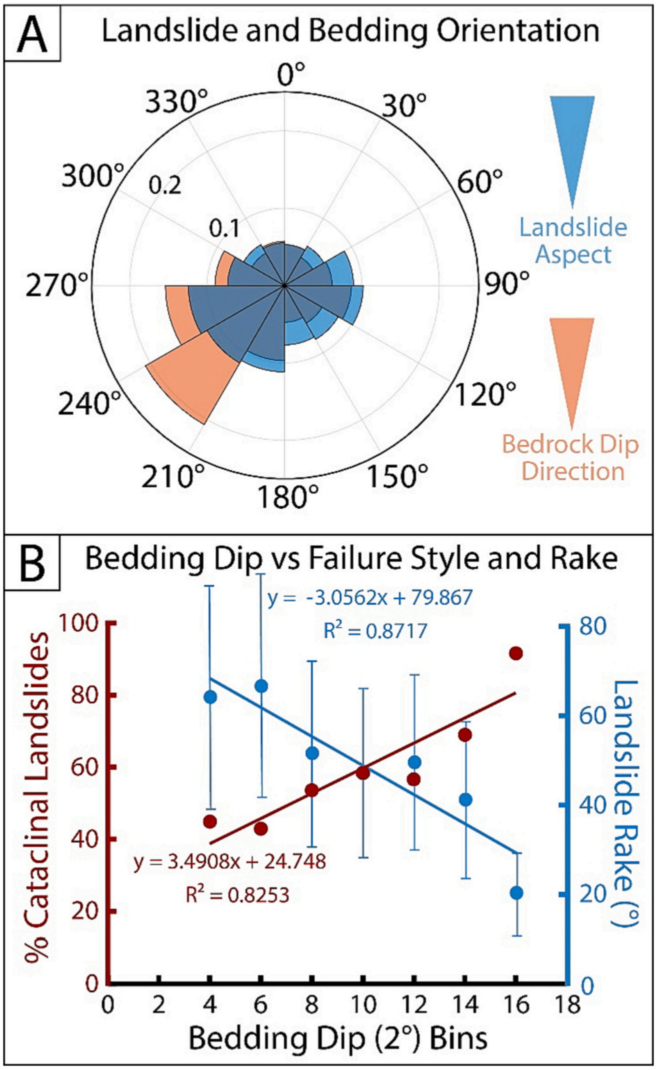

Fig. 8. A. Rose diagram showing probabilistic distributions of bedding dip direction (orange) and landslide aspect (blue). Portions of the bedding dip direction plotted overlapping the aspect data appear dark blue. Probability values sum to 1. B. Plot of Tyee Formation bedding dip magnitude (2° bins breaking on odd integers, i.e. x = 4° represents the 3°-5° bin) versus mean rake per dip bin (blue points with ±1 standard deviation whiskers and best fit linear regression) and percent cataclinal landslides within each dip bin (shown as red points and regression). Landslide rake is defined here as the angular difference between mean landslide aspect and dip direction of bedrock underlying landslide centroid. Cataclinal failures are approximately bedding-parallel, defined as landslides with a mean aspect within 45 degrees of the underlying bedrock dip direction. (For interpretation of the references to colour in this figure legend, the reader is referred to the web version of this article.)

preliminary correlations show no statistically significant relationship between factors promoting landslides, like slope, shaking, and precipitation, we expect additional variability in landslide density could be explained through the incorporation of similar factors. Our results suggest that both intact rock strength (estimated by Schmidt Hammer) and outcrop scale stratigraphic properties are important. Both the proportions and maximum thickness of facies in bimodal layered rocks correlate with landslide density across space, which supports past work linking siltstone proportion to increasing deep-seated landslide density (Roering et al., 2005), and adds new information that suggests thick sandstone beds potentially act to obstruct the formation of landslide slip surfaces due to their substantially higher strength.

Although our model explains much of the variance in overall deep-seated landslide density, and most of the variance in cataclinal landslide density, it performs relatively poorly at predicting the density of non-cataclinal failures (Table 1). In one particularly problematic area in the NE corner of the training area, our combined (all landslides) model significantly underpredicted the real, measured landslide density (Fig. 5). When we examined the orientations of landslides relative to the underlying bedding attitudes in this zone, we found that landslides tend to be randomly oriented, with a high proportion of non-cataclinal landslides. This could potentially be due to the generally shallow dip of the bedding in this region (Fig. 7). This is also a zone characterized by a high density of igneous dikes (Vokes et al., 1951; Struble and Roering, 2021a), the presence of which have been linked to higher landslide density in the Tyee Formation (Roering et al., 2005). However, although detailed mapping of these dikes has been completed for some areas, this level of detail is not comprehensive and may introduce a bias if we attempted to include proximity to these dikes as a variable in our model. Comprehensive mapping of these dikes across the central OCR may serve to improve models by providing a key input to explain even more of the variance in non-cataclinal landslide density.

Overall, our model of landslide density tended to slightly overpredict landslide density in many places and did not exhibit as wide a range of predicted values as the measured values in the training or testing areas (Fig. 5, Fig. 6). Although this lack of extreme values predicted by our model may be an expected effect of any linear regression model, much of this error is likely due to factors that we do not account for in our model, both in terms of inherent material properties and patterns in landslide triggering events.

4.2. *Geologic structure controls deep-seated landslide failure style and influences susceptibility*

Like Roering et al. (2005), we find that structure plays an important role in determining landslide failure style and setting the inherent susceptibility for landslides. However, while Roering et al. (2005) identify structural control on cataclinal landslides in the Tyee Formation, we identify two distinct populations of landslides, cataclinal and non-cataclinal, that respond to distinct drivers of inherent landslide susceptibility and are highly sensitive to dip magnitude. We were able to explain much more of the total variance in landslide density for cataclinal landslides ($R^2 = 0.67$) than for non-cataclinal slides ($R^2 = 0.22$) and found that, of the variables we measured, only sandstone maximum thickness and sandstone strength measured by Schmidt Hammer (S_r) were statistically correlated with non-cataclinal landslide density. This further supports the idea that thick, hard, sandstone beds act as barriers to shear surface development, especially in non-cataclinal slopes where such shear surfaces must cut across many beds. The correlation is weaker, but still statistically significant when cataclinal landslides are considered, perhaps due to the sandstone beds providing tensile strength that must be overcome before any potential landslide mass can begin sliding. Sandstone maximum bedding thickness was not as strongly correlated with the percentage of siltstone in outcrop as siltstone maximum bedding thickness was, and thus it adds an important parameter beyond simple lithologic proportions that helps characterize the rock mass and determine the inherent susceptibility to deep-seated landslides.

We show that while dip magnitude is correlated to increasing deep-seated landslide density, it is a much stronger predictor of landslide type (cataclinal or non-cataclinal landslide). This further confirms the work of Roering et al. (2005), who found deep-seated landslides in the Tyee Formation often fail parallel to the dip direction of fold limbs. Even for shallow dips (>20°), small increases in dip result in a far higher likelihood of landslides failing parallel to bedding. The relatively modest correlation between dip magnitude and landslide density further suggests that deep-seated landslides in the Tyee Formation may occur in flat-lying beds with sufficiently weak rock and may not occur in dipping beds with sufficiently strong rock. However, within dipping beds, landslides that do occur are much more likely to be parallel to bedding, failing along continuous, weak siltstone beds at depth. Similar landslides were triggered after an intense rainstorm in 2014 in Chongqing, China, where bedding contacts between very gently dipping sandstones and mudstones provided slip surfaces for deep (tens of meters) translational bedrock failures (Li et al., 2022). In our study area, deep-seated landslides that occur in bedding dipping at 16° ± 1° have a 92% likelihood to be cataclinal failures - twice as high as landslides that occur in dipping beds of 6° ± 1° (Fig. 8). Subtle changes in dip magnitude result in dramatic changes in landslide behavior, making them larger and much more likely to be structurally controlled, which further underscores the importance of weak, continuous siltstone beds in regulating landslide susceptibility and determining whether slopes fail as large translational slides or smaller rotational slides. This simple relationship between geologic structure and deep-seated landslide failure style, and the ability to interpolate continuous estimates of bedding orientation from dense point measurements, offers promise for further refining hazard models on a more localized scale by identifying which aspects of a drainage are prone to which types of landslide failure.

4.3. *Implications for landscape erosional processes*

Our analysis reveals some regions with few to no deep-seated landslides, which typically exhibit regularly spaced, deeply incised dendritic stream networks and, enigmatically, some of the steepest slopes in the entire study area (Fig. 2). A wealth of literature points to the widespread occurrence of precipitation-driven shallow landslides and debris flows in many of the same regions (Benda, 1990; Schmidt et al., 2001; Coe et al., 2011; Burns, 2020). This prevalence of shallow slope failures in areas with few to no deep-seated failures may suggest distinct erosional process domains are present within the same geologic unit and in the same mountain range, often separated by only a few kms. It is possible that the intra-unit variability we describe in this study is one factor driving the separation of these process domains – perhaps flat lying to gently-dipping portions of the Tyee Mountain Member dominated by thick sandstone beds are able to be eroded into steeper, more highly dissected landscapes. These landscapes would inherently be more prone to shallow landslides and debris flows – processes controlled by factors like slope, precipitation, and root cohesion (Baum et al., 2011), and less dependent on stratigraphic bedrock architecture many meters beneath the landscape surface. In other words, the same geologic and structural factors that would lead to a low inherent susceptibility for deep-seated landsliding may indirectly lead to a higher susceptibility for shallow landsliding by allowing a steeper, more rugged landscape to evolve. This study corroborates the conclusions of Roering et al. (2005), who found local relief decreased as deep-seated landslide density increased. These distinct landslide process domains, separated by hillslope gradient, have also been noted in the folded sandstones and shales that comprise the Chuckanut Formation in Washington State (Schmidt and Montgomery, 1996). This finding has implications for landslide mitigation and risk reduction strategies, which should be specific to the types of landslides affecting different regions and the factors controlling those failure styles (e.g., Grant et al., 2016).

Finally, though not directly considered in this study, lithology and stratigraphic architecture have been shown to play a dominant role in subsurface hydrology, in particular groundwater routing, in ways that promote shallow or deep-seated landslides (Perkins et al., 2017; Marc et al., 2019). In our study area, for example, a hillslope underlain by dipping, thinly bedded, siltstone-rich strata may channel groundwater more quickly to depths at which deep-seated landslides initiate compared to a hillslope underlain by thick, flat-lying sandstone beds. Certain bedding contacts may also act as impermeable hydrologic barriers upon which groundwater may perch, raising local pore-water pressure conditions in the subsurface. Variability in subsurface groundwater routing and conductivity across space may also explain the weak correlation between mean annual precipitation and landslide density (Fig. 2), which only becomes compelling when recent (>1000 year old) landslides are considered (LaHusen et al., 2020). Noting a similarly poor correlation between typhoon rainfall amounts and landslides in Japan, Marc et al. (2019) find that anomalous rainfall (i.e. normalizing event rainfall by 10-year return period rainfall), is far more strongly correlated with landslides. They argue that if hillslopes coevolved with climate, exceeding some statistically extreme, site-specific rainfall amount is the most likely scenario to trigger landsliding. This more nuanced examination of precipitation as a landslide trigger may help explain the variability in landslide density not explained by our model of inherent susceptibility. Though outside the scope of this study, synthesizing data on geologic variability, subsurface groundwater conditions in the Tyee Formation, and an analysis of locally extreme precipitation events may yield a more thorough understanding of the complex drivers of deep-seated landslides in the OCR.

4.4. *Considering landslide preservation*

A potentially important effect that we do not account for in this study is the preservation timescale of deep-seated landslide deposits, and whether that may vary across our study area. After a deep-seated landslide occurs, assuming a single catastrophic failure, the surrounding landscape continues to uplift and erode, eventually removing landslide deposit mass and, with it, the topographic signature of the landslide. In general, we expect the types of landslide deposits we consider in this study to persist for thousands to hundreds of thousands of years (Reneau and Dietrich, 1991; Roering et al., 2001). However, this total preservation time depends on both landscape-wide erosion rates and the depth of the landslide deposit. So, any persistent spatial heterogeneity in erosion rates or landslide depth could influence the number of landslides we map, and therefore the areal landslide density that we regress for in the model presented here. There is some evidence to suggest that bedrock uplift and erosion rates vary within the OCR, despite the lack of mapped crustal faults (Penserini et al., 2017; Struble and Roering, 2021b), and if these rates could be further constrained, we may be able to apply a spatially variable 'preservation factor' to our measured density to account for this effect.

5. Conclusions

We find subtle variations in lithology and structure explain much of the spatial pattern of deep-seated bedrock landslide density and failure style within the Tyee Formation of the central OCR, where traditional drivers of landslide hazards like slope, strong ground motions, and precipitation cannot. The failure of physics-based models to accurately identify deep-seated, landslide-prone terrain in the Tyee Formation when homogenous rock strength parameters are assumed likely reflects a problem unique to deep bedrock landslides. Existing physics-based models developed in the same study area perform well in predicting shallow landslide susceptibility (Montgomery and Dietrich, 1994; Baum et al., 2011) and even forecasting runout and sediment inundation (Reid et al., 2016). However, when landslide failure surfaces extend to tens or hundreds of meters depth - well beyond surficial regolith and soil - bulk rock mass strength and throughgoing heterogeneities may exert as much or more control over landslide hazards than landscape form (e.g., slope, curvature, relief, distance to stream) or soil properties (friction, cohesion, modification by vegetation, etc.). Moreover, in landscapes dominated by large, deep-seated landslide deposits, such as in the Tyee Formation, these topographic factors may be controlled by the presence of landslides, rather than controlling the susceptibility of landslides. Therefore, topography-based models of landslide susceptibility in such environments may effectively identify the forms associated with large deep-seated landslides—reduced surface slope, bench-like terrain, low absolute curvature, occurring in the upper reaches of the drainages, far from streams (e.g., Roering et al., 2005)—without shedding new light on the causal factors actually driving susceptibility.

Although this study targeted a single geologic unit with substantially different rock strengths between facies, similar turbidite sequences underlie many coastal mountain belts around the world and these techniques could also be applied to other sedimentary (e.g., prograding fan) environments conducive to forming rhythmically alternating beds. We show simple field measurements of bedding attitude and characteristics of bedrock outcrops greatly improved our understanding of the drivers and behaviors of deep-seated bedrock landslides within the Tyee Formation. These observations could be adopted quite easily in future local to regional-scale landslide hazard and risk analyses to improve the characterization of spatially variable levels of landslide susceptibility. We demonstrate the emergence of two distinct landslide populations in response to geologic structure, despite the modestly-dipping, gently folded bedrock, where cataclinal landslides become the dominant style of failure above ~8° bedding dip, and account for nearly all landslides when bedding dips exceeds 13°. In more intensely deformed rock than the Tyee Formation, other rock mass characterization schemes such as GSI, RMR, Q, or RMS, as well as joint orientation and spatial density, may further improve landslide type and susceptibility characterization. Ultimately, this work reinforces how heterogeneous bedrock sets the inherent susceptibility to bedrock landsliding and suggests that accounting for intra-unit variability instead of relying solely on mapped geology may be useful in future landslide susceptibility analyses, regardless of the underlying lithology.

Funding statement

This work was entirely funded by the U.S. Geological Survey.

Disclaimer

CRediT authorship contribution statement

Sean R. LaHusen: Writing – review & editing, Writing – original draft, Visualization, Validation, Supervision, Resources, Project administration, Methodology, Investigation, Funding acquisition, Formal analysis, Data curation, Conceptualization. **Alex R.R. Grant:** Writing – review & editing, Visualization, Resources, Methodology, Investigation, Formal analysis, Data curation, Conceptualization.

Declaration of Competing Interest

The authors declare that they have no known competing financial interests or personal relationships that could have appeared to influence the work reported in this paper.

Data availability

Lidar digital elevation data used in this work are openly available from the Oregon Department of Geology and Mineral Industries at https://gis.dogami.oregon.gov/maps/lidarviewer/. Geologic map data and landslides used in this study are available from the original publications cited in text. All field data collected during this work are provided electronically in Supplementary Table 1 and in LaHusen and Grant (2023).

Acknowledgments

We thank Nicolas Mathews, Kevin Schmidt, Josh Roering, and an anonymous reviewer for their constructive and thorough feedback. We also thank the journal editor, Janusz Wasowski, for synthesizing reviewer comments and providing helpful insight.

Appendix A. Supplementary data

Supplementary data to this article can be found online at https://doi.org/10.1016/j.enggeo.2023.107387.

References

Aydin, A., Basu, A., 2005. The Schmidt hammer in rock material characterization. Eng. Geol. 81 (1), 1–14.
Baldwin, E.M., 1955. Geology of the Mary's Peak and Alsea quadrangles, Oregon. U.S. Geological Survey, Oil and Gas Investigations Map, OM-162.
Baldwin, E.M., 1958. Landslide Lakes in the Coast Range of Oregon. Geological Society Oregon Country News Lett, 24, pp. 23–24.
Baldwin, E.M., 1961. Geologic Map of the Lower Umpqua River Area, Oregon. U.S. Geological Survey, Oil and Gas Investigations Map, OM-204.
Baldwin, E.M., 1974. Eocene Stratigraphy of Southwestern Oregon: Oregon Dept. of Geology and Mineral Industries Bulletin, 83, p. 40.
Bandyopadhyay, A., Abdullah, H., 2013. A Laboratory Study of Strong and Weak Sandstones. International Conference on Case Histories in Geotechnical Engineering, 3.
Baum, R.L., Godt, J.W., Coe, J.A., 2011. Assessing susceptibility and timing of shallow landslide and debris flow initiation in the Oregon Coast Range, USA. Ital. J. Eng. Geol. Environ. 825–834.
Benda, L., 1990. The influence of debris flows on channels and valley floors in the Oregon Coast Range, USA. Earth Surf. Process. Landf. 15 (5), 457–466.
Bhandari, B.P., Dhakal, S., 2018. Lithological control on landslide in the Babai Khola watershed, Siwaliks zone of Nepal. Am. J. Earth Sci. 5 (3), 54–64.
Burns, W.J., 2020. Statewide Landslide Information Database for Oregon, Release 4.2: Oregon Department of Geology and Mineral Industries. www.oregongeology.org/slido/index.htm.
Chan, M.A., Dott Jr., R.H., 1983. Shelf and deep-sea sedimentation in Eocene forearc basin, western Oregon—fan or non-fan? Am. Assoc. Pet. Geol. Bull. 67 (11), 2100–2116.
Chen, H., Lin, G.W., Lu, M.H., Shih, T.Y., Horng, M.J., Wu, S.J., Chuang, B., 2011. Effects of topography, lithology, rainfall and earthquake on landslide and sediment discharge in mountain catchments of southeastern Taiwan. Geomorphology 133 (3–4), 132–142.
Coe, J.A., Michael, J.A., Burgos, M.M., 2011. Map of Debris Flows Caused by Rainfall during 1996 in Parts of the Reedsport and Deer Head Point Quadrangles, Douglas County, Southern Coast Range, Oregon. U. S. Geological Survey, Open-File Report 2011-1150.
Dai, F.C., Lee, C.F., 2001. Frequency–volume relation and prediction of rainfall-induced landslides. Eng. Geol. 59 (3–4), 253–266.
Diller, J.S., 1898. Roseburg Folio, Oregon. U.S. Geological Survey, No. 49, 4.
García-Rodríguez, M.J., Malpica, J.A., Benito, B., Díaz, M., 2008. Susceptibility assessment of earthquake-triggered landslides in El Salvador using logistic regression. Geomorphology 95 (3–4), 172–191.
Grant, A., Wartman, J., Abou-Jaoude, G., 2016. Multimodal method for coseismic landslide hazard assessment. Eng. Geol. 212, 146–160.
Grant, A., Struble, W.T., LaHusen, S.R., 2022. Limits to coseismic landslides triggered by Cascadia Subduction Zone earthquakes. Geomorphology 418, 108477.
Guzzetti, F., Cardinali, M., Reichenbach, P., 1996. The influence of structural setting and lithology on landslide type and pattern. Environ. Eng. Geosci. 2 (4), 531–555.
Hammond, C.M., Meier, D., Beckstrand, D., 2009. Paleo-landslides in the Tyee Formation and highway construction, Central Oregon Coast Range. Geol. Soc. Am. Field Guide 15, 481–494.
Heller, P.L., Dickinson, W.R., 1985. Submarine ramp facies model for delta-fed, sand-rich turbidite systems. Am. Assoc. Pet. Geol. Bull. 69 (6), 960–976.
Henriques, C., Zêzere, J.L., Marques, F., 2015. The role of the lithological setting on the landslide pattern and distribution. Eng. Geol. 189, 17–31.
Hess, D.M., Leshchinsky, B.A., Bunn, M., Benjamin Mason, H., Olsen, M.J., 2017. A simplified three-dimensional shallow landslide susceptibility framework considering topography and seismicity. Landslides 14, 1677–1697.
Hoek, E., Carranza-Torres, C., Corkum, B., 2002. Hoek-Brown failure criterion-2002 edition. Proc. NARMS-Tac 1 (1), 267–273.
Hoover, L., 1963. Geology of the Anlauf and Drain Quadrangles, Douglas and Lane Counties, Oregon. U.S. Geological Survey, Bulletin 1122-D.
Keefer, D.K., 1984. Landslides caused by earthquakes. Geol. Soc. Am. Bull. 95 (4), 406–421.
LaHusen, S., 2019. Landslides in Cascadia: Using Geochronometry and Spatial Analysis to Understand the Timing, Triggering and Spatial Distribution of Slope Failures in the Pacific Northwest United States (Doctoral Dissertation).
LaHusen, S.R., Grant, A.R.R., 2023. Bedrock Stratigraphic and Structural Data and Deep-Seated Landslide Density for the Tyee Formation. U.S. Geological Survey data release, OR, USA. https://doi.org/10.5066/P9ATQ0OS.
LaHusen, S.R., Duvall, A.R., Booth, A.M., Grant, A., Mishkin, B.A., Montgomery, D.R., Struble, W., Roering, J.J., Wartman, J., 2020. Rainfall triggers more deep-seated landslides than Cascadia earthquakes in the Oregon Coast Range, USA. Sci. Adv. 6 (38).
Larsen, I.J., Montgomery, D.R., 2012. Landslide erosion coupled to tectonics and river incision. Nat. Geosci. 5 (7), 468–473.
Lee, C.T., Huang, C.C., Lee, J.F., Pan, K.L., Lin, M.L., Dong, J.J., 2008. Statistical approach to earthquake-induced landslide susceptibility. Eng. Geol. 100 (1–2), 43–58.

Li, B., Gao, Y., Yin, Y., Wan, J., He, K., Wu, W., Zhang, H., 2022. Rainstorm-induced large-scale landslides in Northeastern Chongqing, China, August 31 to September 2, 2014. Bull. Eng. Geol. Environ. 81 (7), 1–15.

Lovell, J.P.B., 1969. Tyee formation; a study of proximality in turbidites. J. Sediment. Res. 39 (3), 935–953.

Madin, I.P., 2016. Oregon Geologic Data Compilation, Release 6. Oregon Department of Geology and Mineral Industries. https://www.oregongeology.org/pubs/dds/p-OGDC-6.htm.

Marc, O., Gosset, M., Saito, H., Uchida, T., Malet, J.P., 2019. Spatial patterns of storm-induced landslides and their relation to rainfall anomaly maps. Geophys. Res. Lett. 46 (20), 11167–11177.

Mathews, N., Leshchinsky, B.A., Olsen, M.J., Klar, A., 2019. Spatial distribution of yield accelerations and permanent displacements: a diagnostic tool for assessing seismic slope stability. Soil Dyn. Earthq. Eng. 126, 105811.

Montgomery, D.R., Brandon, M.T., 2002. Topographic controls on erosion rates in tectonically active mountain ranges. Earth Planet. Sci. Lett. 201 (3–4), 481–489.

Montgomery, D.R., Dietrich, W.E., 1994. A physically based model for the topographic control on shallow landsliding. Water Resour. Res. 30 (4), 1153–1171.

Nowicki Jessee, M.A., Hamburger, M.W., Allstadt, K., Wald, D.J., Robeson, S.M., Tanyas, H., Hearne, M., Thompson, E.M., 2018. A global empirical model for near-real-time assessment of seismically induced landslides. J. Geophys. Res. Earth 123, 1835–1859.

Penserini, B.D., Roering, J.J., Streig, A., 2017. A morphologic proxy for debris flow erosion with application to the earthquake deformation cycle, Cascadia Subduction Zone, USA. Geomorphology 282, 150–161.

Perkins, J.P., Reid, M.E., Schmidt, K.M., 2017. Control of landslide volume and hazard by glacial stratigraphic architecture, Northwest Washington State, USA. Geology 45 (12), 1139–1142.

PRISM Climate Group, 2019. Oregon State University. http://prism.oregonstate.edu created 7 Oct.

Reichenbach, P., Rossi, M., Malamud, B.D., Mihir, M., Guzzetti, F., 2018. A review of statistically-based landslide susceptibility models. Earth Sci. Rev. 180, 60–91.

Reid, M.E., Christian, S.B., Brien, D.L., Henderson, S., 2015. Scoops3D—software to analyze three-dimensional slope stability throughout a digital landscape. In: US Geological Survey Techniques and Methods, book, 14.

Reid, M.E., Coe, J.A., Brien, D.L., 2016. Forecasting inundation from debris flows that grow volumetrically during travel, with application to the Oregon Coast Range, USA. Geomorphology 273, 396–411.

Reneau, S.L., Dietrich, W.E., 1991. Erosion rates in the southern Oregon Coast Range: evidence for an equilibrium between hillslope erosion and sediment yield. Earth Surf. Process. Landf. 16 (4), 307–322.

Retallack, G.J., Roering, J.J., 2012. Wave-cut or water-table platforms of rocky coasts and rivers? GSA Today 4–10.

Roering, J.J., Kirchner, J.W., Dietrich, W.E., 2001. Hillslope evolution by nonlinear, slope-dependent transport: Steady state morphology and equilibrium adjustment timescales. J. Geophys. Res. Solid Earth 106 (B8), 16499–16513.

Roering, J.J., Kirchner, J.W., Dietrich, W.E., 2005. Characterizing structural and lithologic controls on deep-seated landsliding: implications for topographic relief and landscape evolution in the Oregon Coast Range, USA. Geol. Soc. Am. Bull. 117 (5–6), 654–668.

Santangelo, M., Marchesini, I., Cardinali, M., Fiorucci, F., Rossi, M., Bucci, F., Guzzetti, F., 2015. A method for the assessment of the influence of bedding on landslide abundance and types. Landslides 12 (2), 295–309.

Santra, M., Steel, R.J., Olariu, C., Sweet, M.L., 2013. Stages of sedimentary prism development on a convergent margin—Eocene Tyee forearc basin, Coast Range, Oregon, USA. Glob. Planet. Chang. 103, 207–231.

Schmidt, K.M., Montgomery, D.R., 1995. Limits to relief. Science 270 (5236), 617–620.

Schmidt, K.M., Montgomery, D.R., 1996. Rock mass strength assessment for bedrock landsliding. Environ. Eng. Geosci. 2 (3), 25–338.

Schmidt, K.M., Roering, J.J., Stock, J.D., Dietrich, W.E., Montgomery, D.R., Schaub, T., 2001. The variability of root cohesion as an influence on shallow landslide susceptibility in the Oregon Coast Range. Can. Geotech. J. 38 (5), 995–1024.

Simpson, R.W., Cox, A., 1977. Paleomagnetic evidence for tectonic rotation of the Oregon Coast Range. Geology 5 (10), 585–589.

Snavely, P.D., Wagner, H.C., MacLeod, N.S., 1964. Rhythmic-bedded eugeosynclinal deposits of the Tyee formation, Oregon Coast Range. Kansas Geol. Surv. Bull. 169, 461–480.

Snavely, P.D., MacLeod, N.S., Wagner, H.C., 1972. Preliminary Bedrock Geologic Map of the Yaquina and Toledo Quadrangles, Oregon. U.S. Geological Survey, Open-File Report 72–352.

Stock, J.D., Montgomery, D.R., Collins, B.D., Dietrich, W.E., Sklar, L., 2005. Field measurements of incision rates following bedrock exposure: implications for process controls on the long profiles of valleys cut by rivers and debris flows. Geol. Soc. Am. Bull. 117, 174.

Struble, W.T., Roering, J.J., 2021a. Dikes of the Central Oregon Coast Range and Southwestern Willamette Valley, Landslide history at Cougar Pass. U.S. Geological Survey, EDMAP.

Struble, W.T., Roering, J.J., 2021b. Hilltop curvature as a proxy for erosion rate: wavelets enable rapid computation and reveal systematic underestimation. Earth Surf. Dyn. 9 (5), 1279–1300.

Struble, W.T., Roering, J.J., Burns, W.J., Calhoun, N.C., Wetherell, L.R., Black, B.A., 2021. The preservation of climate-driven landslide dams in Western Oregon. J. Geophys. Res. Earth 126 (4) e2020JF005908.

Sweet, M.L., Beaubouef, R.T., Beuhler, J., Grove, M., Kloska, M., Mitchell, S., 2007. Distal-basin-floor-fan deposits of the Middle Eocene Tyee Formation, Oregon, USA. AAPG Stud. Geol. 56, 414–417. https://doi.org/10.1306/1240986St56920.

Valagussa, A., Marc, O., Frattini, P., Crosta, G.B., 2019. Seismic and geological controls on earthquake-induced landslide size. Earth Planet. Sci. Lett. 506, 268–281.

Van Westen, C.J., Castellanos, E., Kuriakose, S.L., 2008. Spatial data for landslide susceptibility, hazard, and vulnerability assessment: an overview. Eng. Geol. 102 (3–4), 112–131.

Vokes, E.E., Snavely Jr., P.D., Myers, D.A., 1951. Geology of the Southern and Southwestern Border Areas of the Willamette Valley, Oregon. U.S. Geological Survey, Oil and Gas Investigations Map, OM-110.

Williams, F., McColl, S., Fuller, I., Massey, C., Smith, H., Neverman, A., 2021. Intersection of fluvial incision and weak geologic structures cause divergence from a universal threshold slope model of landslide occurrence. Geomorphology 389, 107795.

Wines, D.R., Lilly, P.A., 2003. Estimates of rock joint shear strength in part of the Fimiston open pit operation in Western Australia. Int. J. Rock Mech. Min. Sci. 40 (6), 929–937.

Wirth, E.A., Grant, A., Marafi, N.A., Frankel, A.D., 2021. Ensemble ShakeMaps for magnitude 9 earthquakes on the Cascadia subduction zone. Seismol. Res. Lett. 92 (1), 199–211.